Materials Research Bulletin 59 (2014) 170–178

Contents lists available at ScienceDirect

Materials Research Bulletin

journal homepage: www.elsevier.com/locate/matresbu

Anisotropic lattice thermal expansion of $PbFeBO_4$: A study by X-ray and neutron diffraction, Raman spectroscopy and DFT calculations

M. Mangir Murshed [a,*], Cecilia B. Mendive [b], Mariano Curti [b], Gwilherm Nénert [c], Patricia E. Kalita [d], Kris Lipinska [e], Andrew L. Cornelius [d], Ashfia Huq [f], Thorsten M. Gesing [a]

[a] Chemische Kristallographie fester Stoffe, Institut für Anorganische Chemie, Universität Bremen, Leobener Straße, D-28359 Bremen, Germany
[b] Departamento de Química, Facultad de Ciencias Exactas y Naturales, Universidad Nacional de Mar del Plata, Dean Funes 3350, B7600AYL, Mar del Plata, Argentina
[c] Institut Laue-Langevin, 6 rue Jules Horowitz, 38042 Grenoble, France
[d] Department of Physics and Astronomy and High-Pressure Science and Engineering Center, University of Nevada Las Vegas, Box 4002, Las Vegas, NV 89154-4002, USA
[e] Department of Mechanical Engineering, University of Nevada Las Vegas, 4505 Maryland Parkway, Box 454009, Las Vegas, NV 89154-4009, USA
[f] Chemical and Engineering Materials Division, Oak Ridge National Laboratory, Oak Ridge, TN 37831-6475, USA

ARTICLE INFO

Article history:
Received 7 December 2013
Received in revised form 17 May 2014
Accepted 4 July 2014
Available online 9 July 2014

Keywords:
Inorganic compounds
Raman spectroscopy
X-ray diffraction
Thermal expansion
Equations-of-state

ABSTRACT

The lattice thermal expansion of mullite-type $PbFeBO_4$ is presented in this study. The thermal expansion coefficients of the metric parameters were obtained from composite data collected from temperature-dependent neutron and X-ray powder diffraction between 10 K and 700 K. The volume thermal expansion was modeled using extended Grüneisen first-order approximation to the zero-pressure equation of state. The additive frame of the model includes harmonic, quasi-harmonic and intrinsic anharmonic potentials to describe the change of the internal energy as a function of temperature. The unit-cell volume at zero-pressure and 0 K was optimized during the DFT simulations. Harmonic frequencies of the optical Raman modes at the Γ-point of the Brillouin zone at 0 K were also calculated by DFT, which help to assign and crosscheck the experimental frequencies. The low-temperature Raman spectra showed significant anomaly in the antiferromagnetic regions, leading to softening or hardening of some phonons. Selected modes were analyzed using a modified Klemens model. The shift of the frequencies and the broadening of the line-widths helped to understand the anharmonic vibrational behaviors of the PbO_4, FeO_6 and BO_3 polyhedra as a function of temperature.

1. Introduction

The crystal structure of mullite-type $PbFeBO_4$ has been known since Park et al. [1], described in space group *Pnma*. A series of isotypic $PbMBO_4$ compounds have been recently reported [2–5] setting the space group as *Pnam* to better understand the physical properties with a conformity to the mullite family members [6,7]. Fig. 1 shows the crystal structure of $PbFeBO_4$ where the infinite chains of edge-sharing FeO_6 octahedra run parallel to the *c*-axis. The FeO_6 octahedra chains are bridged by boron forming a trigonal planar BO_3 group. Between two BO_3 groups a Pb^{2+} cation locates at the apex of a distorted PbO_4 square pyramid, where the $6s^2$ lone electron pair (LEP) of Pb^{2+} cations is stereochemically active. The compound $PbFeBO_4$ has been drawn attention due to its diverse crystal chemical aspects. To describe the magnetic properties of $PbFeBO_4$, where the dominant spin exchange interaction is antiferromagnetic, the edge-sharing FeO_6 octahedra have been considered as a Heisenberg one-dimensional uniform chain model [8]. The nonlinear optical (NLO) properties of $PbFeBO_4$ seem to be promising from two points of view. First, according to the anionic group theory of NLO [9], the planar ionic groups with π-conjugated systems such as trigonal planar BO_3 are responsible for large second harmonic generation (SHG) effects. Second, distortion from the stereochemically active LEP effect on the Pb^{2+} cation can give rise to non-centrosymmetric building units such as PbO_4 leading to SHG. These two non-centrosymmetric local factors in $PbFeBO_4$ may overcome the centrosymmetric constraint for NLO properties.

The thermal expansion behavior ultimately determines the usefulness of many mullite ceramics and mullite refractory

* Corresponding author. Tel.: +49 421 218 63144; fax: +49 421 218 63145.
E-mail addresses: murshed@uni-bremen.de, mmurshed2001@gmail.com (M. M. Murshed).

http://dx.doi.org/10.1016/j.materresbull.2014.07.005
0025-5408/

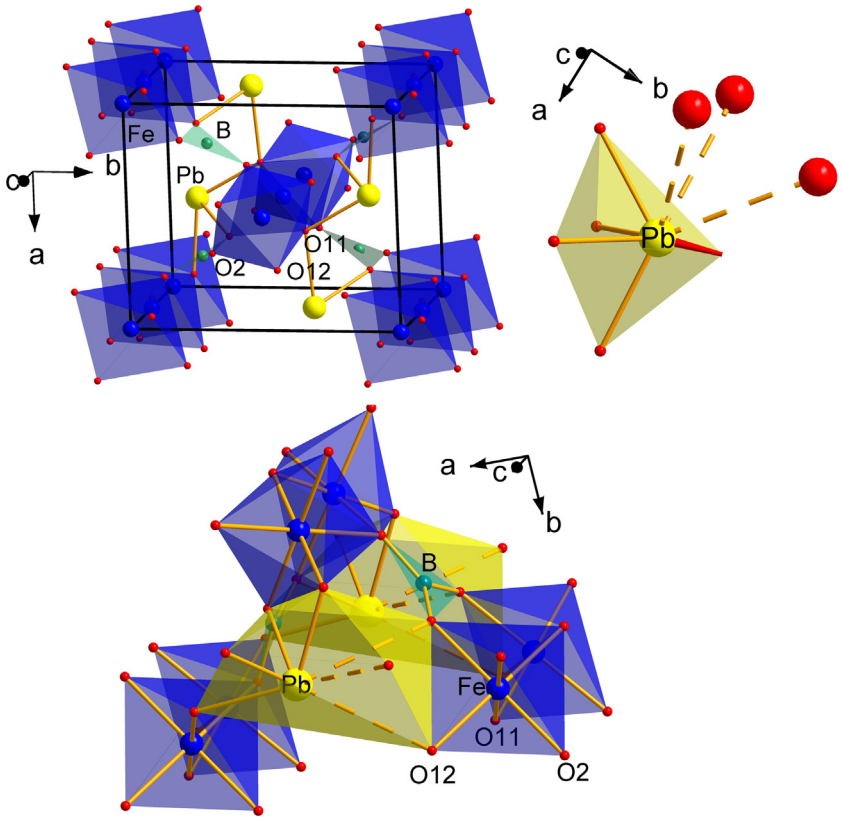

Fig. 1. Crystal structure of mullite-type $PbFeBO_4$ showing edge-sharing FeO_6 octahedra running parallel to the *c*-axis (left), distorted pyramidal PbO_4E (E = lone electron pair) and planar BO_3 and their connectivity.

materials [7]. The thermal behavior of borates mainly stems from their unique B—O bonding strength as either isolated BO_x-polyhedra or bridging BO_x-polyhedral unit. In this report, we study the thermal behavior of $PbFeBO_4$ using temperature-dependent X-ray and neutron diffractions as well as Raman spectroscopy. The combined approach using low-temperature neutron and high-temperature X-ray powder diffraction helps to accurately determine the cell parameters [5] and follow the thermal expansion for a wide temperature range.

2. Experimental methods

2.1. Synthesis

The ^{11}B-enriched polycrystalline $PbFe^{11}BO_4$ was prepared by the glycerin method [10]. Stoichiometric amounts of $Pb(NO_3)_2$, $Fe(NO_3)_2{\cdot}6H_2O$ with 5% excess of $^{11}B(OH)_3$ were mixed with 10 wt. % of glycerin. The mixture was stirred at 353 K till it solidified upon release of NO_x. It was dried at 473 K for 2 h followed by mixing in an agate mortar and then heated at 973 K in a corundum crucible for 24 h.

2.2. X-ray diffraction

The temperature-dependent X-ray powder diffraction data were collected on a Panalytical MPD powder diffractometer using Bragg–Brentano geometry. The instrument was equipped with a secondary Ni filter, CuKα radiation, a X'Celerator multi strip detector and an Anton Paar HTK1200N heating chamber. The sample was placed on a flat corundum holder having a small evaporation channel that served for optimum space during thermal expansion of $PbFeBO_4$. Diffraction was carried out between 300 K and 700 K with a ramping slice of 10 K. Each diffraction pattern was recorded from 10° to 135° 2θ with a step size of 0.0167° and a 50 s/step total data collection time. The fluorescence radiation of the iron bearing sample could be seen in the powder pattern with a slightly increased background, however, it did not pose any inconveniences for Rietveld calculations. The fundamental parameter approach, where the fundamental parameters were fitted against a LaB_6 standard material, was applied for the Rietveld refinement using "Diffrac^{Plus} Topas 4.2" software (Bruker AXS GmbH, Karlsruhe). For this purpose the starting atomic coordinates were taken from the neutron diffraction quality data.

2.3. Neutron diffraction

Low-temperature neutron time-of-flight (TOF) data were collected on the Powgen high resolution diffractometer at Oak Ridge National Laboratory, USA. Approximately 5 g of ^{11}B enriched $PbFe^{11}BO_4$ powder sample was loaded in a vanadium container of 8 mm diameter. Temperature-dependent data were collected from 10 K to 90 K in 5 K steps followed by 10 K steps up to 300 K using a close cycle refrigeration system. Longer datasets (1.5 h) were collected at 10, 100, 200 and 300 K which covered a *d*-spacing range from 30 pm to 620 pm, while the rest of the data were collected for 10 min spanning a *d*-spacing between 40 pm and 360 pm. The Rietveld refinement on the powder data were performed using GSAS [11]. It is worth noting that Powgen uses a TOF profile function that varies from the standard profile function originally derived for GSAS [12]. The variation in peak shape and peak position with the Powgen diffractometer is calculated using a function related to thermal and epithermal components of the neutron spectrum and implemented in GSAS to accurately

determine the metric parameters. During the Rietveld refinement the scale factor, absorption coefficient, two profile shape parameters, lattice parameters, fractional coordinates of the atoms and their displacement parameters were optimized. The thermal expansion behavior of $PbFeBO_4$ has been studied using the composite dataset of the low temperature neutron (10 K–300 K) and high temperature (300 K–700 K) X-ray powder diffractions; a linear correction was made by an optimization between the X-ray and neutron data at 300 K.

2.4. Raman spectroscopy

The temperature-dependent Raman spectra were recorded on a Horiba Jobin Yvon (LabRam ARAMIS) micro-Raman spectrometer equipped with a laser working at 785 nm. The use of a 50× long working distance objective (Olympus) with a numerical aperture of 0.55 provides a focus spot of about 2 μm diameter when closing the confocal hole to 200 μm. Raman spectra were collected in the range between 80 cm^{-1} and 1500 cm^{-1} with a spectral resolution of approximately 1.0 cm^{-1} using a grating of 1800 grooves/mm and a thermoelectrically cooled CCD detector (Synapse, 1024 × 256 pixels). The spectral positions were calibrated against the Raman mode of Si before and after the sample measurements. The position of the Si peak was repeatedly measured against the Rayleigh line (0.0 cm^{-1}) yielding a value of 520.7 ± 0.1 cm^{-1}. The linearity of the spectrometer was calibrated against the emission lines of a neon lamp. For the low-temperature measurements a pressed pellet of the powder sample was placed in the Linkam cooling stage (THMS600) attached with a LNP95 cooling pump that provides continuous flow of liquid nitrogen. The measurements were carried out between 78 K and 300 K with temperature steps of 5 K and holding time of 5 min. The high-temperature spectra were performed on a heating stage (Linkam L-TS1500) between 300 K and 713 K in steps of 10 K and holding time of 10 min. Each spectrum was baseline corrected and fitted with pseudo-Voigt line-shape with the 'LAMP' software suite [13]. The pseudo-Voigt line-shape is a convolution of the natural Lorentzian lineshape of the phonon with the instrumental Gaussian broadening. The instrumental broadening was checked using different slit configurations and measured for λ = 585.249 nm emission line of a neon lamp, which was fitted with a pure Gaussian line-shape providing the line-width, Γ_G = 1.88(1) cm^{-1}. Then the intrinsic phonon line-widths were calculated using the Voigt profile approximation: $\Gamma_v \approx 0.5346\ \Gamma + (0.2166\ \Gamma^2 + {\Gamma_G}^2)^{0.5}$, where Γ and Γ_L refer to the observed and Lorentzian intrinsic phonon line-width, respectively.

The pressure-dependent Raman spectra were measured in a backscattering configuration with a Horiba Jobin-Yvon T64000 triple-grating confocal Raman spectrometer using micro-mode. The 514.532 nm line of a Spectra Physics Stabilite 2018 Ar–Kr laser was used for sample excitation less than 10 mW power at the sample to avoid burning. A liquid nitrogen cooled CCD detector (Symphony, 2048 × 512 pixels) was used for recording the spectra. The incoming and scattered light was focused and collected with an Olympus microscope objective (20× LWD), leading to a theoretical 1.7 μm diameter focal spot and a length of the focal region of a few micrometer. Raman spectra were collected in the range between 10 cm^{-1} and 1300 cm^{-1} with a spectral resolution of approximately 1 cm^{-1}, using three gratings of 1800 grooves/mm working in subtractive mode. Signal integration times were 100–600 s, with multiple acquisitions per pressure point, and with longer acquisition times for increasing pressure measurements. Band positions, determined from peak fitting are accurate to ±4 cm^{-1} for broad/overlapped bands and ±1 cm^{-1} for the sharper bands.

Micro grains of the sample were compressed in a symmetric type diamond anvil cell (DAC), from ambient pressure up to 20.4 GPa in several pressure steps at ambient temperature. A Rhenium gasket was pre-indented to a thickness of ~50 μm using diamonds with 250 μm diameter culets. The sample chamber consisted of a 90 μm diameter hole, drilled in the pre-indented rhenium gasket. To ensure quasi-hydrostatic pressure conditions, compression was carried out with a 4:1 methanol–ethanol mixture for pressure ≤10 GPa, and with a modified 16:3:1 methanol–ethanol–water mixture for >10 GPa. For accurate pressure readings during compression ruby microspheres were placed in the sample chamber and used to measure pressure using the Mao pressure scale [14]. A second method for pressure determination was based on the shift of the high-frequency edge of the Raman band of diamond, which corresponds to the Raman shift of the anvil culet due to the normal stress [15]. The interval between a pressure increase and the measurement of spectra was kept at several minutes allowing for the pressure inside the sample chamber to equilibrate. Spectra were decomposed into individual Lorentzian or mixed Gaussian–Lorentzian bands using LabSpec 5.78.24 software (Jobin-Yvon Horiba).

2.5. DFT calculations

Periodic calculations were performed with the crystalline orbital program CRYSTAL09 [16,17], employing the PW1PW hybrid Hartree Fock–Density Functional Theory (HF–DFT) method [18]. All structures were optimized starting from the experimental crystallographic data. The basis sets were taken from the CRYSTAL website database [19]. The Monkhorst–Pack shrinking factor was set to 4 after checking energy convergence of the structures, that is, 27 independent *k*-points in the irreducible Brillouin zone were taken. A high spin ferromagnetic configuration was used for Fe^{3+} cation in $PbFeBO_4$.

Geometry optimizations were done under a hydrostatic constant pressure as implemented in CRYSTAL09 [17]. By changing the pressure to the desired value, the different pressure-dependent unit-cell volumes were obtained. The constant pressure constrained geometry optimizations were performed at 0, 5, 10, 15, 20 and 30 GPa. By varying the lattice parameters (as implemented in CRYSTAL09) and fitting the energy we calculated the bulk modulus (K_T = 62.05(1) GPa) and the zero-pressure volume at 0 K (V_0 = 351.23(1) × 10^6 pm^3). It is important to note here that both the experimental values of V_0 and K_T differ slightly from the corresponding DFT values within standard deviation.

Harmonic frequencies of the optical Raman modes at the Γ-point of the Brillouin zone at 0 K were calculated by computing numerically the second derivatives of the energy with respect to the atomic positions, and diagonalizing the mass-weighted Hessian matrix in Cartesian coordinates, as implemented in CRYSTAL09 [17,20]. The Raman phonon modes were given as an output of the calculations. The mode-Grüneisen parameters were calculated from the linear fit of the pressure dependent experimental and DFT Raman data.

3. Results and discussion

3.1. Lattice thermal expansion

The thermal expansion of the metric parameters is shown in Fig. 2; respective fit models and energy contributions are given as insets. A detail of the modeling is described later in this section. Although measurable antiferromagnetic reflections appear elsewhere at low temperatures [1], there is no significant thermal expansion anomaly. Therefore, the applied model does not take magnetostriction into account due to smooth (within the uncertainly) change of the metric parameter between 10 K and 700 K. Both the *b*- and *c*-cell parameters show positive thermal

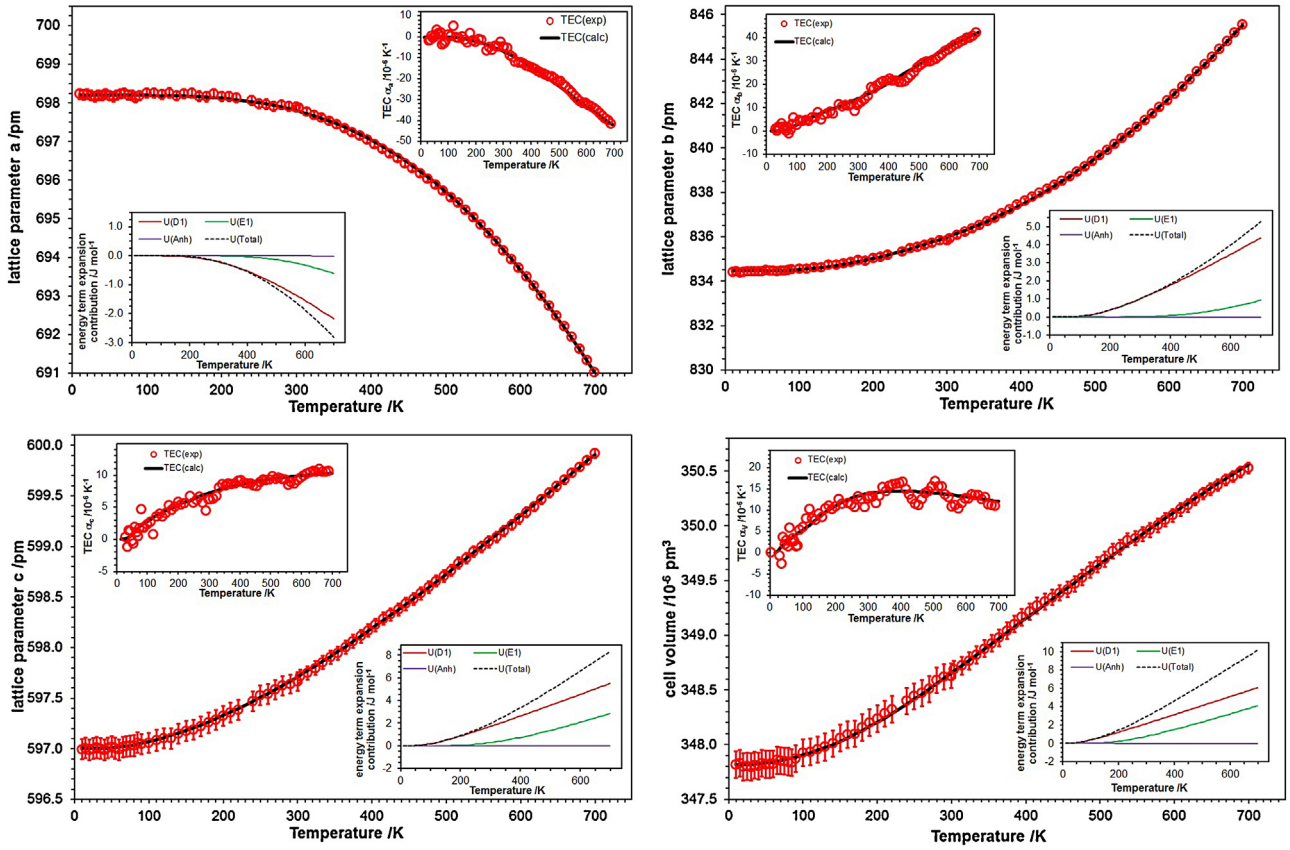

Fig. 2. Thermal expansion of the $PbFeBO_4$ metric parameters (3σ e.s.d.'s) together with the DEA model simulations (solid line). Temperature-dependent thermal expansion coefficients (TEC) of the corresponding metric parameters and the model calculation (solid line) are given inset. Calculated energy contributions multiplied with their respective expansion (+1) or contraction (−1) effect from different additive terms (Eq. (3)) are also given inset.

expansion, while the *a*-cell parameter negative thermal expansion with a total positive non-linear cell volume expansion. Below 300 K the *a*-cell parameter contracts only slightly, and the nonlinear shape of the volume thermal expansion is mainly due to the expansion of the *b*- and *c*-cell parameters. Both *b*- and *c*-cell parameters show low-temperature saturations below 50 K and that of *a*-cell parameter at about 100 K. As a consequence, the cell-volume plot shows slight sigmoid behavior with respect to temperature.

The thermal expansion of solids can be adequately modeled using both Einstein harmonic and Debye quasi-harmonic models. In the Einstein harmonic model the atoms in a solid are independent oscillators and free from other sources of dynamical entropy. The Debye quasi-harmonic model also assumes independent oscillators, however, with altered frequencies. None of the thermal expansion coefficient (TEC) of the metric parameters saturate at a temperature-independent region for the observed range (Fig. 2, inset), which is assumed to be associated with intrinsic anharmonicity leading to anisotropic and anomalous thermal expansion of $PbFeBO_4$. The volume thermal expansion clearly departs from the model fitted either with Debye or Einstein models with single characteristic temperature in particular at high temperature as anharmonicity becomes increasingly significant. Trials with a mixture of single-Debye and single-Einstein model did not improve the fitting. However, inclusion of an anharmonicity term sufficiently restores the agreement between the model and the observed data. We recently applied a model taking both the Debye and Einstein approximations along with an intrinsic anharmonicity term [21] in the additive frame of the model to describe the change of the internal energy of the crystal as a function of temperature [4,22]. The volume thermal expansion can be expressed using Grüneisen thermoelastic parameters [23]:

$$\gamma = \frac{\alpha_V V K_T}{C_V} \tag{1}$$

where γ is the thermodynamic Grüneisen parameter, C_V is the isochoric specific heat capacity. Assuming that the γ and K_T are temperature independent integration of Eq. (1) with respect to temperature leads to the following expression for the temperature-dependent volume thermal expansion in terms of the internal energy of the crystal:

$$V(T) = V_0 + \frac{U(T)}{Q} \tag{2}$$

This expression holds the first-order Grüneisen approximation to the zero pressure equation of state, where adjustable constant $Q = K_T/\gamma$ and $U(T)$ is the internal energy due to thermal lattice vibration. We further extend the energy term and generalized Eq. (2) taking harmonic, quasi-harmonic and anharmonic vibrational contributions to $U(T)$ as:

$$M(T) = M_0 + \sum_{i=1}^{d} k_{\mathrm{Di}} U_{\mathrm{Di}}(T) + \sum_{i=1}^{e} k_{\mathrm{Ei}} U_{\mathrm{Ei}}(T) + k_{\mathrm{A}} U_{\mathrm{A}}(T) \tag{3}$$

where $M(T)$ refers to any of the temperature dependent metric parameters ($V(T)$, $a(T)$, $b(T)$ and $c(T)$), k_{Di}, k_{Ei} and k_{A} are adjustable fitting parameters given in Table 1, contributing to Debye (U_{Di}), Einstein (U_{Ei}) and anharmonic (U_{A}) internal energies, respectively, where

Table 1
Median values (3σ e.s.d.'s) resulting from the fitting of the temperature-dependent metric parameters of $PbFeBO_4$.

M	*V*	*a*	*b*	*c*
Model[a]	DEA	DEA	DEA	DEA
M_0[b]	347.8(3)	698.2(7)	834.4(5)	597.0(2)
$k_{D1}/10^{-12}$	2.7(2)	−15.9(15)	13.6(9)	3.1(1)
θ_{D1}/K	235(19)	1962(184)	791(50)	406(13)
$k_{E1}/10^{-12}$	4.6(4)	−44.0(41)	43.7(28)	2.78(9)
θ_{E1}/K	683(54)	2648(249)	2259(143)	1108(34)
$k_A/10^{-12}$	479(38)	0.28(3)	178(11)	2.98(9)
$a_A/10^{-5}\,K^{-1}$	1	1	1	1
θ_A/K	θ_{D1}	θ_{D1}	θ_{D1}	θ_{D1}

[a] DEA = Debye–Einstein-anharmonic model as given in Eq. (3) for $d = 1$ and $e = 1$.
[b] Metric parameters *a*, *b*, *c* and *V* at 0 K are given in pm and 10^6 pm^3, respectively. Estimated uncertainty is given in the parentheses.

$$U_{Di}(T) = \left[9Nk_BT\left(\frac{T}{\theta_{Di}}\right)^3\int_0^{\theta_{Di}/T}\frac{x^3}{e^x-1}dx\right] \quad (4)$$

$$U_{Ei}(T) = \left[\frac{3Nk_B\theta_{Ei}}{e^{(\theta_{Ei}/T)}-1}\right] \quad (5)$$

$$U_A(T) = \left[a_A\frac{3Nk_B\theta_A^2}{24T}\left[Te^{(3\theta_A/T)} + 9Te^{(2\theta_A/T)} - 12\theta_Ae^{(2\theta_A/T)} - 9Te^{(\theta_A/T)} - 12\theta_Ae^{(\theta_A/T)} - T\right]\left[\left(e^{(\theta_A/T)}-1\right)^3\right]^{-1}\right] \quad (6)$$

N refers to the number of atoms per unit cell ($N = 28$), k_B is Boltzmann constant, θ_{Di} and θ_{Ei} are the characteristic Debye ($\theta_{Di} = hc\omega_{Di}/k_BT$) and Einstein ($\theta_{Ei} = hc\omega_{Ei}/k_BT$) temperatures. Setting

$$\theta_A = \frac{\sum_{i=1}^{d}k_{Di}\theta_{Di}}{\sum_{i=1}^{d}k_{Di}} \quad (7)$$

we transformed the harmonic oscillator frequency into Debye arbitrary phonon spectrum (quasi-harmonic) [21]. a_A is the anharmonicity parameter which is fixed to $10^{-5}\,K^{-1}$ for all the models we present in this report using $d = 1$ and $e = 1$ (DEA-model). The integral term of the Debye function is evaluated numerically. For modeling the *a*-cell parameter both the fitting constants k_{D1} and k_{E1} were refined to negative values caused by the observed negative thermal expansion. The second and the third terms of Eq. (3) consist of isothermal anharmonicity taking isothermal Grüneisen parameters whereas the fourth term contains isochoric anharmonicity with temperature-dependent Grüneisen parameter. Therefore, although Eq. (3) is an extension of the Eq. (2) it breaks down the Grüneisen first approximation. Consequently, the zero pressure 0 K metric parameter (M_0) must contain the respective quantum mechanical zero-point energy, respectively, $9Nk_B\theta_D/8$, $3Nk_B\theta_E/2$ and $Nk_Ba_A(\theta_A)^2/8$ for Debye, Einstein and the anharmonicity term.The thermal expansion coefficients α_a, α_b, α_c and α_V for, respectively, *a*, *b*, *c* and cell volume are numerically calculated and compared with the corresponding models (Fig. 2, insets). The thermal expansion coefficients (TEC) also showed no definite saturation at any given temperature, indicating either non-Debye or non-Einstein solid. This also supports the use of an anharmonicity term in the model, since it gives excellent descriptions of the temperature-dependent metric parameters, in particular in the mid-range of the cell-volume thermal expansion, where both the Debye and Einstein model suffers from temperature limitation. The lattice anisotropy factor (A_{latt}) was calculated using the following correlation and given in Fig. 3,

$$A_{latt}(T) = |a(T) - b(T)| + |b(T) - c(T)| + |c(T) - a(T)| \quad (8)$$

which increases with increasing temperature with a steep change at high temperature. This indicates that the change of the microscopic properties (e.g., axis-directional asymmetry of the oscillator frequency) in the $PbFeBO_4$ crystal leads to enhanced anharmonicity at high temperature.

3.2. Raman spectroscopy

Factor group analysis predicts 36 Raman active modes for the selective site symmetries in the space group *Pnam*. Fitting of the spectrum at ambient condition required 24 bands between 80 cm^{-1} and 1400 cm^{-1}. The technical limitation of the instrument

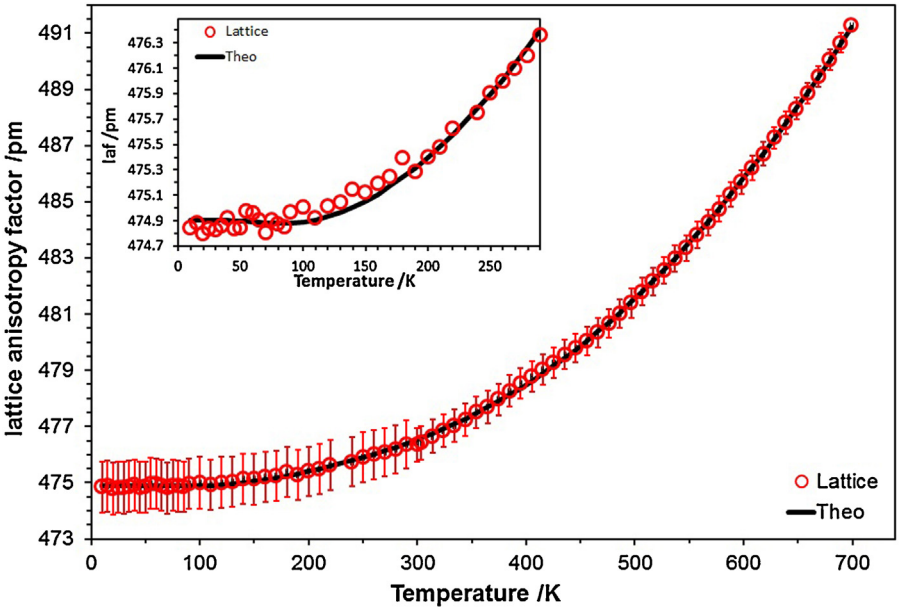

Fig. 3. Temperature-dependent anisotropy of the metric parameters (3σ e.s.d.'s). The magnified low temperature region was shown in the inset.

Table 2
Calculated and experimental Raman phonon frequencies of $PbFeBO_4$ together with their corresponding mode-Grüneisen parameters.

$(\omega_i)_{DFT}$	$(\omega_i)_T$ $T = 78$ K	$(\omega_i)_T$ $T = 298$ K	$(\omega_i)_P$ $P = 0.0001$ GPa $T = 298$ K	Pressure for $(\gamma_i)_p$/GPa	$(\gamma_i)_P$	$(\gamma_i)_{DFT}$	Irr. Rep.	Assignment
56.8	–	–	54.63	0–5.6	−0.88	−0.68(0)	AG	Pb—O stretch
	–	–	54.63	6.7–17.5	0.28	1.61(27)	AG	Pb—O stretch
67.6	–	–	67.9	0–17.5	−0.13	−0.03(24)	B1G	O—Pb—O wagg
70.5	–	–	66.9	0–5.6	−2.22	−1.57(0)	B2G	O—Pb—O wagg
	–	–	66.9	6.7–11.4	2.3	1.43(35)	B2G	O—Pb—O wagg
95.9	94.2	92.2	92.5	–	–	0.80(14)	B3G	Pb—O stretch
	–	–	98.8	0–17.5	2.36	–	AG	Pb—O stretch
97.4	101.8	100.0	100.7	0–17.5	2.43	2.16(3)	AG	Pb—O stretch
112.8	111.9	109.3	–	–	–	0.41(3)	B3G	Pb—O stretch
162.4	156.8	148.8	–	–	–	−2.72(36)	AG	O—Pb—O scissor
194.9	193.7	191.0	191.1	0–7.8	−0.91	0.26(0)	B3G	O—Pb—O scissor
202.9	196.7	193.3	193.4	0–7.8	−0.25	−0.55(8)	B2G	O—Pb—O scissor
203.7	201.9	–	–	–	–	0.01(5)	B1G	O—Pb—O rock
269.7	267.0	259.6	261.8	0–6.7	−0.45	−0.39(6)	B1G	O—Fe—O symm + O—Pb—O assym
269.7	–	–	261.8	7.8–17.5	0.86	–	B1G	O—Fe—O symm + O—Pb—O assym
270.3	270.8	264.4	269	0.5–7.8	0.14	0.36(5)	B3G	O—Fe—O scissor + O—Pb—O scissor
274.5	–	–	266	0.5–5.6	−0.21	−0.26(0)	B2G	O—Pb—O assym stretch
	–	–	266	6.7–20.4	0.63	0.46(0)	B2G	O—Pb—O assym stretch
298.5	293.0	289.8	287.9	0–20.4	0.28[a]	0.35(4)	AG	O—Fe—O scissor
325.4	319.4	316.1	–	–	–	0.71(0)	AG	O—Fe—O symm + O—Pb—O wagg
330.1	–	–	–	–	–	0.68(2)	B2G	O—Fe—O symm + O—Pb—O twist
350.2	358.3	356.7	–	–	–	0.76(1)	AG	Pb—O stre + O—Fe—O sci
367.2	–	–	–	–	–	0.54(6)	B3G	O—Fe—O symm
373.8	–	–	359.9	0–20.4	0.81[a]	0.59(3)	B1G	O—Fe—O rock
433.7	437.5	434.1	432.3	0–20.4	0.50	0.48(0)	B3G	O—Fe—O rock
505.0	496.4	484.6	491.7	0–20.4	0.29	0.28(7)	B2G	O—Pb—O twist
507.9	506.1	494.9	505	1.5–14.6	0.26	0.27(7)	AG	O—Fe—O symm
538.9	–	–	–	–	–	0.52(3)	B3G	O—Pb—O sci + O—Fe—O symm
574.4	–	–	556.5	0–17.5	0.30	0.29(7)	B1G	O—Pb—O wagg
625.1	614.1	609.9	634.0	0–20.4	0.17[a]	0.24(1)	B1G	O—B—O scissor
628.4	–	–	–	–	–	0.01(2)	B3G	O—B—O scissor
636.1	633.5	632.2	–	–	–	0.24(3)	AG	O—B—O scissor
682.8	668.7	667.1	665.1	0–20.4	0.20	0.24(3)	B2G	O—B—O scissor
695.6	697.4	695.9	676	12.1–20.4	0.06	−0.08(1)	AG	O—B—O wagg
725.8	–	–	687	9.7–20.4	0.45	0.14(0)	BG3	O—B—O wagg
942.1	929.5	925.9	925.5	0–20.4	0.35	0.15(1)	BG3	B—O symm stretch
957.1	942.8	942.1	–	–	–	0.18(2)	AG	B—O symm stretch
1221.0	1180.1	1177.3	1176.0	0–20.4	0.30[a]	0.13(1)	AG	B—O assym stretch
1238.4	1183.8	–	1184.3	0–11.4	0.39	0.32(3)	B2G	B—O assym stretch
1240.2	1193.3	1191.3	1195.7	3.7–11.4	0.39	0.31(4)	B1G	B—O asymm stretch
1319.9	–	–	–	–	–	0.08(1)	B3G	B—O asymm stretch

$(\omega_i)_{DFT}$, $(\omega_i)_T$ and $(\omega_i)_P$ refer to Raman phonon frequency calculated by DFT at 0 K and 0 GPa, obtained from temperature-dependent and pressure-dependent experiments, respectively. $(\gamma_i)_{DFT}$ and $(\gamma_i)_P$ are mode-Grüneisen parameters obtained from DFT and pressure-dependent experiments, respectively.

[a] Corresponding mode-Grüneisen parameter were obtained from experimental data exhibiting small non-linearity but fitted with a straight line.

and the low intense bands reduce the number of experimentally observed modes compared to the theoretical ones (Table 2). The number of experimentally observed modes is further reduced due to thermal emission at high temperature followed by increasing background contribution to the spectra. The observed modes at ambient conditions associated with the FeO_6 and PbO_4 polyhedra conform closely to the corresponding predicted frequencies, however, most of the BO_3 modes showed reasonable deviations. These deviations can be explained by the fact that the theoretical calculations were carried out on natural boron and the experimental observation on the ^{11}B-enriched samples. The pressure derivatives $(\partial\omega_i/\partial P)$ were used to calculate the mode-Grüneisen parameters, $\gamma_i = B_0(1/\omega_{i0})(\partial\omega_i/\partial P)$, where B_0 = isochoric bulk modulus, ω_{i0} = mode frequency at zero pressure (Table 2). The disagreements of some γ_i both in values and signs (positive/negative) might arise from several sources: (i) different values of the bulk modulus ($(B_0)_{DFT} = 62.04(1)$ GPa, $(B_0)_{EXP} = 70.5(7)$ GPa); (ii) non-linear behavior of the frequency shifts with respect to pressure and (iii) high-spin configuration of the FM phase considered for DFT. To minimize the discrepancies into an acceptable comparison we checked γ_i at different pressure limits ($P_{DFT} = 0$–20 GPa, $P_{EXP} \sim 0$–20 GPa). At least 25% of the total observed modes showed non-linear response to pressure. Thus modes with non-linear pressure-derivative and negative mode-Grüneisen parameters (Table 2) were not used for anharmonic analyses. The temperature-dependent Raman shift of the most frequencies exhibit normal behavior as usual in ionic crystals, that is, frequency decreases and line-widths increases with increasing temperature. For anharmonic analyses six phonons ω_i were chosen, where $i = 94$, 194, 293, 437, 634 and 1183 at 0 K (corresponding to the Raman shift in cm^{-1}), respectively, assigned to Pb—O stretching, O—Pb—O scissoring, O—Fe—O rocking, O—Fe—O scissoring, O—B—O scissoring and B—O asymmetric stretching of the corresponding PbO_4, FeO_6 and BO_3 polyhedra (Table 2). Such selection in particular for temperature-dependent anharmonic analyses of the modes seems to be difficult due to some inherent complications. Beside the temperature effects, most of the modes are not well separated and they are characteristically prone to merge and overlap due to non-linearity of γ_i. Moreover, the spin-phonon interaction at the respective antiferromagnetic regions further complicates the scenario. For example, Fig. 4 shows anomalous hardening/softening of two modes in a broad range at low temperature. That is, sharp features corresponding to two T_N points at 120 K and 280 K, respectively, for long range and short range antiferromagnetic (AFM) ordering [1] were not observed so far. ω_{i0} has been obtained from the extrapolation of the

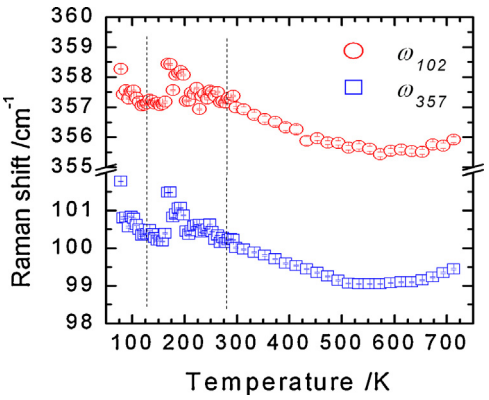

Fig. 4. Temperature-dependent phonon anomaly shown by two phonon modes at the antiferromagnetic region (vertical dashed lines).

low-temperature data excluding the possible AFM region (120–280 K). Thus for the anharmonic model analysis the spin-phonon interaction region was not considered. Anharmonicity of the phonon modes involve phenomena beyond those of the independent phonons. The higher-order phonon-phonon interactions are the main source of the anharmonic behavior, which causes the frequency (energy) of the harmonic oscillators in a crystalline solid to be temperature dependent. This temperature dependence arises in two different ways: (i) a pure-volume effect associated with the thermal expansion and (ii) a pure-temperature effect that is present even at a constant volume. To reveal the temperature-dependent Raman mode behavior, we follow the proposed models [24–26] which has been recently applied to mullite-type $Bi_2Ga_4O_9$ system [22]. The frequency of a Raman phonon can be modeled according to the following expression:

$$\omega_i(T) = \omega_{i0} + \Delta\omega_i(T) \tag{9}$$

$\Delta\omega_i(T)$ refers to total shift and is an additive term of two contributions as given in Eq. (10):

$$\Delta\omega_i(T) = \Delta\omega_i^{\mathrm{latt}}(T) + \Delta\omega_i^{\mathrm{anh}}(T) \tag{10}$$

$\Delta\omega_i{}^{\mathrm{anh}}(T)$ refers to the frequency shift due to phonon-phonon interactions; the term is also known as the pure temperature contribution. $\Delta\omega_i{}^{\mathrm{latt}}(T)$ is the frequency shift due to volume thermal expansion. Assuming that both B_0 and γ_i (the reason for selecting the modes with positive γ_i for analysis) are temperature independent, the term $\Delta\omega_i{}^{\mathrm{latt}}(T)$ can be expressed as:

$$\Delta\omega_i^{\mathrm{latt}}(T) = \omega_{i0}\left\{\exp\left[-\int_0^T \gamma_i\alpha_V(T)\mathrm{d}t\right] - 1\right\} \tag{11}$$

The observed $\Delta\omega_i{}^{\mathrm{anh}}(T)$ is modeled using the Balkanski model [24], considering the phonon decay into two channels namely, the 3-phonon and 4-phonon interactions:

$$\Delta\omega_i^{\mathrm{anh}}(T) = A\left(1 + 2/\left(e^{hc\omega_{i0}/2k_BT} - 1\right)\right) + B\left(1 + 3/\left(e^{hc\omega_{i0}/3k_BT} - 1\right) + 3/\left(e^{hc\omega_{i0}/3k_BT} - 1\right)^2\right) \tag{12}$$

A and B are damping factors given in Table 3, representing the relative probability of the occurrence of the 3-phonon (cubic decay) and 4-phonon (quartic decay) processes contributing to the frequency shift, respectively. The model convincingly describes our observed data for the anharmonic phonon contribution to the frequency shift (Fig. 5). All modes smoothly soften, where $\Delta\omega_i{}^{\mathrm{anh}}(T)$ dominates over $\Delta\omega_i{}^{\mathrm{latt}}(T)$ for the whole temperature range. The observed low temperature spectral data appear above and below the model line, which demonstrates hardening and softening of those modes, respectively. Modes ω_{94}, ω_{194} and ω_{634} slightly harden while ω_{293} and ω_{437} moderately soften along with a significant softening of ω_{1183} in the AFM region; a definite softening/hardening for ω_{634} cannot be ascertained due to scattering. In other words, softening occurred in FeO_6 and BO_3, and hardening in PbO_4 polyhedra. This behavior is not associated with the lattice anomalies, but with a possible spin-phonon coupling caused by phonon modulation of the super-exchange integral. Because the term $\Delta\omega_i{}^{\mathrm{latt}}(T)$ is smooth due to the theoretical nature of $\alpha_V(T)$ at the AFM region. Mode ω_{293} hardly requires 4-phonon contribution and the model poorly fits to ω_{634} due to scattering of the data associated with low thermal response to the O—B—O bending. Mode ω_{1183} requires high damping factors (A and B), which are about one order of magnitude higher than those required by other modes considered. It demonstrates that the intrinsic anharmonicity for the thermal expansion mainly comes from the BO_3 group. It is known that thermal expansion anomaly in many metal borates as well as in glasses essentially relates to the anharmonic vibrational properties of the associated borate groups. This observation further justifies the anharmonic term to be taken in the lattice thermal expansion model as also considered in some lithium borates [27].

The intrinsic line-width of a Raman phonon mode in a defect-free sample mainly comes from two terms: (i) electron-phonon and (ii) anharmonic phonon-phonon interactions. The electron-phonon interaction mainly appears at temperatures below 10 K and was not considered to analyze the temperature-dependent mode broadening as shown in Fig. 5. The temperature-dependent line-widths of the modes have been modeled using the Balkanski approach [25], however, with an extended form (e.g., [22,28]) as expressed in Eq. (13):

$$\Gamma_i(T) = \Gamma_{i0} + C\left(1 + 2/\left(e^{hcw_{i0}/2k_BT} - 1\right)\right) + D\left(1 + 3/\left(e^{hcw_{i0}/3k_BT} - 1\right) + 3/\left(e^{hcw_{i0}/3k_BT} - 1\right)^2\right) \tag{13}$$

Factor Γ_{i0} refers to a damping contribution that commences from the inherent defect or impurity scattering at 0 K. The second and third term correspond to symmetric decay of 3-phonon and 4-phonon decay with anharmonic constants C and D, respectively.

Table 3
Selective temperature-dependent Raman phonon modes of $PbFeBO_4$ with the fitting parameters used for Eqs. (12) and (13).

ω_{i0}/cm^{-1}	$(\gamma_i)_T$	A/cm^{-1}	B/cm^{-1}	Γ_0/cm^{-1}	C/cm^{-1}	D/cm^{-1}
94.3	0.80	−0.2193(1)	−0.0021(1)	1.20(1)	0.0658(1)	–
194	0.26[a]	−0.6710(1)	−0.0315(1)	1.28(1)	1.138(1)	0.0050(1)
293.2	0.35[a]	−1.152(1)	−0.0066(1)	2.679(2)	1.793(1)	0.0226(1)
437.1	0.50	−0.4337(1)	−0.3043(1)	2.02(1)	4.199(1)	0.3312(1)
633.7	0.25	−0.8826(3)	−0.0540(1)	4.653(1)	2.751(2)	0.2342(1)
1183	0.30	−7.7619(5)	−3.156(7)	1.183(1)	1.221(1)	4.43(1)

[a] Mode-Grüneisen parameter was found to be negative from the pressure-dependent experiments, the corresponding positive values calculated by DFT were taken for fitting.

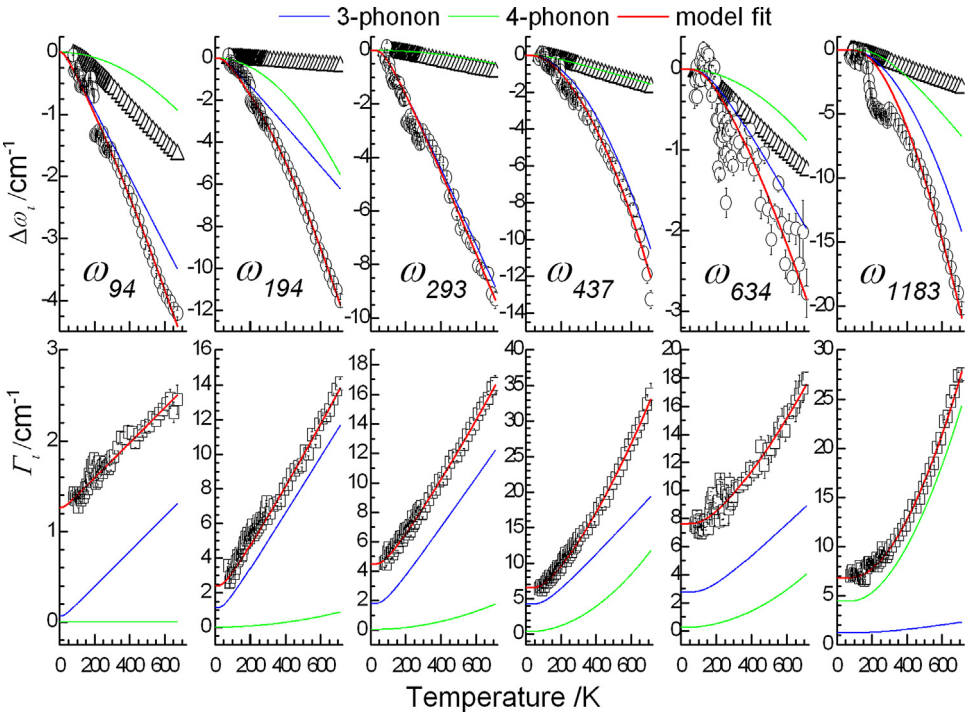

Fig. 5. Temperature-dependent phonon frequencies and intrinsic line-widths changes of some representative $PbFeBO_4$ Raman modes. The triangle (Δ), circle (◯) and square (□) refer to frequency shift due to volume contribution ($\Delta\omega_i^{latt}$), anharmonic contributions ($\Delta\omega_i^{anh}$) and observed line-width (Γ_i), respectively. The solid lines represent model calculations based on phonon-phonon interactions.

Fig. 5 shows the temperature-dependent change of the line-widths along with the model lines for different contributions; the fitting constants are given in Table 3. Thermal emission particularly hampers and limits the line-width analyses due to mode disappearance, overlapping and increasing background. Table 3 shows the substantial contributions of both the 3-phonon and 4-phonon processes to frequency broadening of the modes. The theoretical model satisfactorily fits most observed data. A smooth non-linear change of the line-width followed by a high-temperature linear steep rise explains the usual symmetric decay of the modes. Γ_{1183} requires higher anharmonic constants of 4-phonon contributions than that of 3-phonon; the higher values justify the higher anharmonicity of the BO_3 group. At the AFM region Γ_{293} lies above the model fit, showing slight broadening with an overall sigmoid behavior. Thus Γ_{293} clearly departs from the symmetric channels showing evidence of phonon renormalization between 3-phonons and 4-phonons at the AFM region.

4. Conclusion

The Raman phonon modes related to PbO_4 cover an extensive low energy range (<300 cm^{-1}). Most of these modes are associated with the asymmetry of the vibrational potential (anharmonic phonon) since they clearly show non-linear pressure derivatives together with negative mode-Grüneisen parameter (Table 2). The BO_3 group keeps its rigidity at any temperature and FeO_6 octahedra are distorted; both these two polyhedra locate close to stereochemically active lone electron pair of Pb^{2+} cation. Therefore, $PbFeBO_4$ is anharmonic at the fundamental level like many solids with hard and soft modes. From the energy plot (Fig. 2d, inset) it is clear that the contribution of the anharmonicity started as early as about 100 K and taking the perturbative anharmonic term [21] can model the thermal expansion of the metric parameters for the temperature range between 10 K and 700 K. Due to lack of phonon dispersion information, the negative thermal expansion of *a*-cell parameter cannot be straightforwardly explained in terms of the corresponding phonons with negative Grüneisen parameters.

Acknowledgements

We gratefully acknowledge the Deutsche Forschungsgemeinschaft (DFG) for the financial support through the mullite-LEP project GE1981/4-1. TMG especially acknowledges the DFG for a support in the Heisenberg program (GE1981/3-1). Part of the research conducted at ORNL's Spallation Neutron Source was sponsored by the Scientific User Facilities Division, Office of Basic Energy Sciences, US Department of Energy. High-pressure Raman spectroscopy in diamond anvil cell was carried out using experimental facilities of FAME-Tech Labs (University of Nevada Las Vegas, Dept. of Mechanical Engineering) which are supported by DOE-EERE under Award No. DE-FG 3606GO8636 and Award No. EE-0000269. Work at UNLV is supported by DOE award No. DEFG36-05GO08502. The UNLV, HiPSEC is supported by the US Department of Energy, National Nuclear Security Administration, under Cooperative Agreement DE-FC08-01NV14049. CBM is a member of the research staff of CONICET and thanks ANPCyT (Arg.) for the financial support PICT-2683. MC is grateful to CONICET for the doctoral scholarship.

References

[1] H. Park, R. Lam, J.E. Greedan, J. Barbier, Synthesis, crystal structure, crystal chemistry, and magnetic properties of $PbMBO_4$ (M = Cr, Mn, Fe): a new structure type exhibiting one- dimensional magnetism, Chem. Mater. 15 (2003) 1703.
[2] M.M. Murshed, A. Rusen, R.X. Fischer, Th. M. Gesing, Transition-metal substitution in $PbAlBO_4$: synthesis, structural and spectroscopic studies of manganese containing phases, Mater. Res. Bull. 47 (2012) 1323.
[3] M.M. Murshed, R.X. Fischer, Th. M. Gesing, The role of the Pb^{2+} lone electron pair for bond valence sums analysis in $PbMBO_4$ (M = Al, Mn and Fe) mullite-type compounds, Z. Kristallogr. 227 (2012) 580.
[4] Th. M. Gesing, C.B. Mendive, M. Curti, D. Hansmann, G. Nénert, -P.E. Kalita, K.E. Linpinska, A. Huq, A.L. Cornelius, M.M. Murshed, Structural properties of

mullite-type $Pb(Al_{1-x}Mn_x)BO_4$, Z. Kristallogr. (2013), doi:http://dx.doi.org/10.1524/zkri.2013.1640.
[5] M.M. Murshed, G. Nénert, Th. M. Gesing, Crystal structure of mullite-type $PbMn_{0.5}Al_{0.5}BO_4$ determined by combined X-ray and neutron diffraction data, Z. Kristallogr. NCS 227 (2012) 285.
[6] R.X. Fischer, H. Schneider, The mullite-type family of crystal structures, in: H. Schneider, S. Komarneni (Eds.), Mullite, Wiley-VCH, Weinheim, 2005, pp. 1–46.
[7] H. Schneider, Mechanical properties of mullite, in: H. Schneider, S. Komarneni (Eds.), Mullite, Wiley-VCH, Weinheim, 2005, pp. 141–149.
[8] H.-J. Koo, M.-H. Whangbo, Density functional investigation of the magnetic properties of $PbMBO_4$ (M = Cr, Mn, Fe), Solid State Commun. 149 (2009) 602.
[9] C. Chen, G. Liu, Recent advances in nonlinear optical and electro-optical materials, Ann. Rev. Mater. Sci. 16 (1986) 203.
[10] Th. M. Gesing, R.X. Fischer, M. Burianek, M. Mühlberg, T. Debnath, C.H. Rüscher, J. Ottinger, J. -Ch. Buhl, H. Schneider, Synthesis and properties of mullite-type $(Bi_{1-x}Sr_x)2(M1_{1-y}M2_y)4O_{9-x}$ (M = Al, Ga, Fe), J. Eur. Ceram. Soc. 31 (2011) 3055.
[11] B.H. Toby, EXPGUI, a graphical user interface for GSAS, J. Appl. Cryst. 34 (2001) 210.
[12] R.B. von Dreele, J.D. Jorgensen, C.G. Windsor, Rietveld refinement with spallation neutron powder diffraction data, J. Appl. Crystallogr. 15 (1982) 581.
[13] D. Richard, M. Ferrand, G.J. Kearley, Analysis and visualisation of neutron-scattering data, J. Neutron Res. 4 (1996) 33.
[14] H.K. Mao, P.M. Bell, J.W. Shaner, D.J. Steinberg, Specific volume measurements of Cu, Mo, Pd, and Ag and calibration of the ruby R1 fluorescence pressure gauge from 0.06 to 1 Mbar, J. Appl. Phys. 49 (1978) 3276.
[15] Y. Akahama, H. Kawamura, Pressure calibration of diamond anvil Raman gauge to 310 GPa, J. Appl. Phys. 100 (2006) 043516.
[16] R. Dovesi, R. Orlando, B. Civalleri, C. Roetti, V.R. Saunders, C.M. Zicovich-Wilson, CRYSTAL: a computational tool for the ab initio study of the electronic properties of crystals, Z. Kristallogr. 220 (2005) 571.
[17] R. Dovesi, V.R. Saunders, C. Roetti, R. Orlando, C.M. Zicovich-Wilson, F. Pascale, B. Civalleri, K. Doll, N.M. Harrison, I.J. Bush, P. D' Arco, M. Llunell, CRYSTAL09 User's Manual, University of Torino, Torino, 2009.
[18] T. Bredow, A.R. Gerson, Effect of exchange and correlation on bulk properties of MgO, NiO, and CoO, Phys. Rev. B 61 (2000) 5194.
[19] http://www.crystal.unito.it/Basis_Sets.
[20] F. Pascale, C.M. Zicovich-Wilson, F. Lopez, B. Civalleri, R. Orlando, R. Dovesi, The calculation of the vibrational frequencies of crystalline compounds and its implementation in the CRYSTAL code, J. Comput. Chem. 25 (2004) 888.
[21] A.R. Oganov, P.I. Dorogokupets, Intrinsic anharmonicity in equations of state and thermodynamics of solids, J. Phys.: Condens. Matter 16 (2004) 1351.
[22] M.M. Murshed, Th. M. Gesing, Anisotropic thermal expansion and anharmonic phonon behavior of mullite-type $Bi_2Ga_4O_9$, Mat. Res. Bull. 48 (2013) 3284.
[23] D.C. Wallace, Thermodynamics of Crystals, Dover, New York, 1998.
[24] P.G. Klemens, Anharmonic decay of optical phonons, Phys. Rev. 148 (1966) 845.
[25] M. Balkanski, R.F. Wallis, E. Haro, Anharmonic effects in light scattering due to optical phonons in silicon, Phys. Rev. B 28 (1983) 1928.
[26] T. Lan, X. Tang, B. Fultz, Phonon anharmonicity of rutile TiO_2 studied by Raman spectrometry and molecular dynamics simulations, Phys. Rev. B 85 (2012) 094305.
[27] A. Senyshyn, H. Boysen, R. Niewa, J. Banys, M. Kinka, Y. Burak, V. Adamiv, F. Izumi, I. Chumak, H. Fuess, High-temperature properties of lithium tetraborate $Li_2B_4O_7$, J. Phys. D: Appl. Phys. 45 (2012) 175305.